

The internal structure of Mercury's core inferred from magnetic observations

I. Wardinski^{1,2}, H. Amit², B. Langlais² & E. Thébault²

¹Institut de Physique du Globe de Strasbourg, Université de Strasbourg/EOST, CNRS, UMR 7516,

Strasbourg, France

²Laboratoire de Planétologie et Géodynamique, Université de Nantes, Université d'Angers, CNRS, UMR

6112, Nantes, France

Key Points:

- We model Mercury's internal magnetic field from MESSENGER data with spherical harmonics
- Our core field model contains non-axisymmetric features from which we make inferences of Mercury's internal structure.
- We estimate Mercury's inner core radius of ~ 500 - 660 km and a corresponding thickness of a top stratified layer of ~ 880 - 500 km.

Abstract

Previous models of Mercury’s core magnetic field based on high altitude data from first MESSENGER flybys revealed an axisymmetric. Here we use low altitude MESSENGER data covering the entire mission period to construct spherical harmonic models based on various spatial norms. Although we find a dominantly axisymmetric field, our models nevertheless include detectable deviations from axisymmetry. These non-axisymmetric features appear at high latitudes, resembling intense geomagnetic flux patches at Earth’s core-mantle boundary. Based on this core field morphology, we then attempt to infer Mercury’s internal structure. More specifically, assuming that Mercury’s high-latitude non-axisymmetric features are concentrated by downwellings at the edge of the planet’s inner core tangent cylinder, and accounting for the presence of a stably stratified layer at the top of Mercury’s core, we establish a relation between the inner core size and the thickness of the stratified layer. Considering plausible ranges, we propose that Mercury’s inner core size is about 500-660 km, which corresponds to a stratified layer thickness of 880-500 km, respectively.

1 Introduction

Based on Mariner and MESSENGER satellite missions, it was found that Mercury’s internal magnetic field is very weak, dipole dominated, largely axisymmetric and with a magnetic equator shifted northward with respect to the geographic equator at mid-latitudes of the northern hemisphere (Ness et al., 1974; Ness, 1979; Anderson et al., 2011, 2012; Johnson et al., 2012; Oliveira et al., 2015; Thébaud et al., 2018; Wardinski et al., 2019), which is challenging to explain in terms of core structure and dynamics. In addition, several studies of Mercury’s interior based on analyses of MESSENGER gravity field measurements and libration data suggested that the top of Mercury’s outer core is thermally stratified (Smith et al., 2012; Dumberry & Rivoldini, 2015). Likely, this layer is comprised of FeS, but its phase (liquid or solid) remains uncertain. Thermal stratification implies that the heat flux at the core surface is sub-adiabatic, which has important implications for the inner core solidification and the magnetic field generation.

Numerical dynamo simulations may provide further insight into Mercury’s core structure. Possible scenarios include deep-seated dynamos below a thick stable layer (Christensen, 2006; Christensen & Wicht, 2008; Takahashi et al., 2019), thin-shell dynamos (Stanley et al., 2005) and dynamos with a thin stratified layer (Stanley & Mohammadi, 2008).

47 While numerical dynamos with a stably stratified layer at the top of the shell can ex-
48 plain Mercury’s weak magnetic field and its axisymmetry, additional ingredients are needed
49 to explain the northward shift of the magnetic equator. Numerical dynamos with im-
50 posed heterogeneous heat flux in the form of equatorial cooling at the outer boundary
51 (Cao et al., 2014; Tian et al., 2015) lead to a convective instability and an offset of the
52 magnetic equator, but their magnetic fields are too energetic and non-axisymmetric. Dou-
53 ble diffusive convection phenomena have also been considered to explain Mercury’s mag-
54 netic field. These phenomena occur when the convection is driven by two sources of buoy-
55 ancy, i.e. temperature and composition (Manglik et al., 2010). Recently, Takahashi et
56 al. (2019) showed that a double-diffusive convecting shell surrounded by a thick ther-
57 mally stably stratified layer can generate Mercury-like magnetic fields. Furthermore, nu-
58 merical dynamo models of Mercury’s magnetic field provide estimates of the size of Mer-
59 cury’s inner core. Cao et al. (2014) suggested an inner core radius smaller than 1000 km.
60 Based on geodetic analyses Dumberry and Rivoldini (2015) gave an upper limit on the
61 inner core size of 650 km, with the outer core dynamics partly consisting of snow for-
62 mation.

63 These different scenarios of Mercury’s dynamo lead to characteristics that should
64 be testable by observations of space-borne magnetometers like MESSENGER and Bepi-
65 Columbo. A careful processing and analysis of magnetic field measurements taken in plan-
66 etary environments is crucial for the identification of such magnetic field characteristics.

67 Mainly, two techniques have been applied to study Mercury’s magnetic fields: po-
68 tential field methods such as spherical harmonics (Uno et al., 2009; Wardinski et al., 2019),
69 spherical caps (Thébault et al., 2018) or equivalent source dipoles (Oliveira et al., 2015)
70 that restrict the analysis to those observations obtained in a source free region, and (re-
71 duced) parametric models that infer the magnetic dipole moment from the space probe’s
72 magnetic equator crossing, i.e. where the radial field B_r is zero, far from the planet (An-
73 derson et al., 2012; Johnson et al., 2012). The latter method provides models with a re-
74 duced set of parameters and is popular because of its relative independence of the data
75 distribution. Data used for these reduced parametric models sampled the magnetic field
76 in the magnetospheric region, with a considerable electrical current density that requires
77 additional assumptions about the geometry and distribution of local current systems (Con-
78 nerney & Ness, 1988). In contrast, Uno et al. (2009) showed by inverting synthetic data
79 from numerical dynamo simulations that a spherical harmonic analysis can recover the

80 large-scale magnetic field from hemispherical uneven data distribution, as single MES-
81 SENDER flybys, when data are taken in a source-free region. The resolution of finer de-
82 tails of the magnetic field needs, off course, numerous orbital tracks.

83 In this study magnetic field data are used to derive field models that may constrain
84 the internal structure of a planet. The downward continuation of a magnetic field model
85 to the core surface reveals patterns of magnetic flux. In particular, the latitude at which
86 intense flux patches are concentrated may indicate the size of the inner core. Intense flux
87 concentrations near the intersection of the inner core tangent cylinder are prominent in
88 the geomagnetic field for at least the last 400 years (e.g. Jackson et al., 2000) and pos-
89 sibly over the past tens of millennia (see Panovska et al., 2019, and references therein).
90 Numerous studies explored the kinematics as well as the dynamical origin of intense high-
91 latitude flux patches in geomagnetic field models and numerical dynamos (Bloxham et
92 al., 1989; Christensen et al., 1998; Amit et al., 2010, 2011; Peña et al., 2016; Olson et
93 al., 2018). The latitude at which these flux concentrations occur has been related to the
94 change of the dynamical regime at the tangent cylinder that is coaxial with the rotation
95 axis and tangential to the inner core boundary (Gubbins & Bloxham, 1987), while the
96 longitude at which these flux patches occur may be controlled by thermal core-mantle
97 interactions (Bloxham & Gubbins, 1987).

98 Here we will use inferences from the Earth’s core to carefully establish the relation
99 between the latitude of intense magnetic flux patches and the tangent cylinder intersec-
100 tion with the core-mantle boundary (CMB), including possible errors associated with
101 time-dependence and variability from one patch to another. We will then account for the
102 existence of stratification to relate the depth of the stable layer with the radius of the
103 inner core for a given latitude of magnetic flux patches. This relation will be implemented
104 for the case of Mercury’s magnetic field.

105 The aim of this study is twofold: First, we explore to what extent intermedie-
106 scale spatial features of Mercury’s magnetic field can be retrieved from the MESSEN-
107 GER data by applying a spherical harmonic analysis; Second, we aim to infer the inter-
108 nal structure of Mercury’s core and the convective state of its dynamo. The paper is or-
109 ganized as follows: The description of the data and their selection is given in section 2,
110 section 3 briefly describes the spherical harmonic modeling method, and results are pro-
111 vided in section 4. Implications for the generation of Mercury’s core field and the struc-

112 ture of its core are discussed in section 5. We summarize our main findings in section
 113 6.

114 2 Data selection

115 The MESSENGER spacecraft was in orbit around Mercury from 18 March 2011
 116 to 30 April 2015. The orbit of MESSENGER was highly eccentric, with periapsis rang-
 117 ing from 200 to 500 km over the north polar region, and apoapsides of > 12700 km above
 118 the southern hemisphere. This highly eccentric orbit led to an uneven data distribution,
 119 where only measurements over the northern hemisphere are assumed to be inside the mag-
 120 netospheric cavity which allow adequate modeling of Mercury’s internal magnetic field
 121 (Oliveira et al., 2015). All local times are covered within 88 (terrestrial) days.

122 Here, we selected data from a satellite altitude range of 300 to 1000 km during lo-
 123 cal night-time. This provides a data set which shows no crustal magnetic signatures and
 124 the least contamination from magnetospheric and exospheric magnetic fields (Wardinski
 125 et al., 2019), which are strong at the planet’s day-side. The altitude selection criterion
 126 guarantees that the analyzed magnetic field measurements are within the magnetospheric
 127 cavity: 1000 km is smaller than the averaged subsolar distance of the magnetopause lo-
 128 cation (Winslow et al., 2013), while the lower limit excludes data from the beginning and
 129 the end of the MESSENGER mission. Oliveira et al. (2019) showed that the crustal mag-
 130 netic signal is small-scale, and weak in amplitude at 40 km altitude. Therefore, at 300
 131 km altitude signals due to crustal magnetization are assumed to be negligible at large
 132 length scales.

133 3 Method

134 We seek to fit MESSENGER observations of Mercury’s magnetic field by a poten-
 135 tial that is parameterized using spherical harmonics, i.e.

$$\begin{aligned}
 V = a \sum_{l=1}^{L_{\text{int}}} \sum_{m=0}^l \left\{ (g_l^m \cos(m\phi) + h_l^m \sin(m\phi)) \left(\frac{a}{r}\right)^{l+1} P_l^m(\cos\theta) \right\} \\
 + a \sum_{l=1}^{L_{\text{ext}}} \sum_{m=0}^l \left\{ (q_l^m \cos(m\phi) + s_l^m \sin(m\phi)) \left(\frac{r}{a}\right)^l P_l^m(\cos\theta) \right\}, \quad (1)
 \end{aligned}$$

136 where a is Mercury’s radius (2440 km). r is the radial distance from Mercury’s center,
 137 θ the colatitude and ϕ the longitude. $P_l^m(\cos\theta)$ are the Schmidt semi-normalized asso-
 138 ciated Legendre functions, where l is the degree and m the order. L_{int} and L_{ext} are the

139 truncation degrees of the spherical harmonic expansions for the internal and external field,
 140 respectively. The Gauss coefficients $\{g_l^m, h_l^m\}$ and $\{q_l^m, s_l^m\}$ represent the internal and
 141 external magnetic field, respectively. These model parameters are estimated by a least
 142 squares fit to data collected during a given time interval. In the following, we outline de-
 143 tails of our modeling technique, which is sometimes called smoothed inversion (Holme
 144 & Bloxham, 1996; Uno et al., 2009). The selection of night-time data with altitude less
 145 than 1000 km allows a robust separation of external and internal magnetic field sources.
 146 For the spherical harmonic expansion, we set $L_{\text{int}} = 10$ and $L_{\text{ext}} = 1$. As stated in
 147 Wardinski et al. (2019) external magnetic fields with $L_{\text{ext}} > 1$ cannot be estimated with
 148 confidence.

149 3.1 Model priors

150 For a linear least squares problem the model vector \mathbf{m} containing the Gauss coef-
 151 ficients is found at the minimum of an objective function

$$\Theta(\mathbf{m}) = (\mathbf{y} - \mathbf{A}\mathbf{m})^T \mathbf{C}_e^{-1} (\mathbf{y} - \mathbf{A}\mathbf{m}) + \lambda_S (\mathbf{m}^T \mathbf{C}_m^{-1} \mathbf{m}), \quad (2)$$

152 where \mathbf{y} is the data vector, \mathbf{A} a design matrix, \mathbf{C}_e the data error covariance matrix and
 153 \mathbf{C}_m the prior model covariance matrix (Jackson, 1979; Gubbins, 1983) which is controlled
 154 by a Lagrange multiplier. The misfit of the model is computed by

$$\hat{\sigma} = \sqrt{\frac{\sum_{i=1}^N (y_i - \hat{y}_i)^2}{N - 1}}, \quad (3)$$

155 where \hat{y}_i is the model value for given observation y_i .

156 Our method to find the Gauss coefficients utilizes prior constraints to reduce the
 157 ambiguity of the data inversion. The application of priors to constrain the inversion of
 158 MESSENGER data to obtain a model of Mercury’s magnetic field is justified by their
 159 uneven hemispherical distribution. Primarily, the prior should emphasize the large-scales
 160 of Mercury’s magnetic field. We test the performance of four different priors of the spa-
 161 tial complexity of the model’s field morphology. These priors are usually formulated as

162 model norms:

$$\begin{aligned}
 \text{Norm 1 : } \oint B^2 dS|_{r=c} &= (l+1) \left(\frac{a}{c}\right)^{(2l+4)} \\
 \text{Norm 2 : } \oint B_r^2 dS|_{r=c} &= \frac{(l+1)^2}{2l+1} \left(\frac{a}{c}\right)^{(2l+4)} \\
 \text{Norm 3 : } \oint (\nabla_h B_r)^2 dS|_{r=c} &= \frac{l(l+1)^3}{2l+1} \left(\frac{a}{c}\right)^{(2l+6)} \\
 \text{Norm 4 : } \oint F dS|_{r=c} &= \frac{(l+1)(2l+1)(2l+3)}{l} \left(\frac{a}{c}\right)^{(2l+3)} \leq Q.
 \end{aligned} \tag{4}$$

163 In Norm 4 of (4) F is the field intensity and Q is the mean CMB heat flux. In all these
 164 expressions (4), Mercury's core radius is $c = 2060$ km (Wardinski et al., 2019). Norm
 165 1 minimizes the power of the magnetic field for higher spherical harmonic degrees, and
 166 therefore it steepens the slope of its power spectrum. Norms 2 and 3 smooth the radial
 167 magnetic field and its horizontal gradient, respectively (Shure et al., 1982). Norm 4 is
 168 different from the other norms as it may include prior knowledge of the heat flux at Mer-
 169 cury's core surface, which is due to the Ohmic dissipation of the radial field B_r at the
 170 core surface (Gubbins, 1975). However, there are no observations of the heat flux at Mer-
 171 cury currently available. Therefore, Norm 4 acts merely as a constraint to stabilize the
 172 solution of the inversion like the other norms. All norms dim the amplitude of small-scale
 173 field features, though at different ways, hence support the large-scale morphology of the
 174 magnetic field. Among these norms, this effect is most strongly imposed by Norm 3, where
 175 the attenuation scales with l^3 .

176 The strength of the prior constraint is controlled by the Lagrange multiplier λ_S .
 177 The resulting model is determined by varying the strength of the prior to be in optimal
 178 balance between data misfit and model smoothness. This optimal balance is usually found
 179 for the λ_S at the knee of their trade-off or L-curves.

180 3.2 Iterative modeling scheme

181 To find the model parameters, we adopt an iterative re-weighting scheme that con-
 182 sists of three steps. At a first step, we determine a model that is based on data cover-
 183 ing the MESSENGER's entire mission interval at Mercury. Data are weighted equally,
 184 to form the initial error covariance matrix, \mathbf{C}_e , in (2). We assign an initial error of 1.6
 185 nT to each datum which corresponds to the upper limit of the instrument's resolution
 186 (Anderson et al., 2007). At a second step, individual differences between each data and

187 corresponding values of the initial model are computed, to provide an update of \mathbf{C}_e and,
 188 third, to derive the final model with the updated error covariance matrix. The residual
 189 amplitude, and therefore \mathbf{C}_e , depends directly on the Lagrange multiplier λ_S ; In order
 190 to obtain a close trade-off curve for each norm, this iterative re-weighting scheme is ap-
 191 plied for each setting of λ_S . In total we derive a large number of models for each norm.
 192 We select the model at the knee of each norm trade-off curve.

193 A closer inspection of the residuals reveals anomalous tracks that show significant
 194 larger residual amplitudes than others. The cause for these large residuals remains un-
 195 clear, but could be related to instrument errors and/or data processing errors. However,
 196 these data are automatically down-weighted and rejected from the model derivation when
 197 the misfit is larger than 2σ .

198 3.3 Robustness of the solutions

199 There are a few diagnostics to evaluate the robustness and confidence of the inver-
 200 sion results. First, we analyze the resolution matrix of the model \mathbf{m} , to obtain a mea-
 201 sure of model parameter significance. The resolution matrix is given by

$$\mathbf{R} = (\mathbf{A}^T \mathbf{C}_e^{-1} \mathbf{A} + \lambda_s \mathbf{C}_m^{-1})^{-1} \mathbf{A}^T \mathbf{C}_e^{-1} \mathbf{A}, \quad (5)$$

202 where the diagonal elements of \mathbf{C}_m are defined in (4). Ideally, this matrix would be an
 203 identity matrix. Due to inadequacy of the data, a regularization scheme must be applied
 204 in the solving process to obtain a stable solution. This is reflected in the form of the res-
 205 olution matrix. A value of the resolution near 1 means that a model parameter is wholly
 206 determined by the data, whereas a low resolution, i.e. values ~ 0.1 , means that the model
 207 is mostly controlled by the prior information. The trace of the resolution matrix $Tr(\mathbf{R})$
 208 can be broadly interpreted as the degree of freedom of the model and as the number of
 209 model parameters resolved by the inversion (Tarantola, 1987).

210 Characteristics and diagnostics of the field models are listed in Table 1. All mod-
 211 els widely agree in their statistical properties, and mostly differ in their numbers of re-
 212 solved parameters. The lowest number of resolved parameters is found for Norm 3, as
 213 it more strongly damps contributions of higher spherical harmonic degrees than other
 214 norms and therefore reduces the degree of freedom most strongly.

Table 1. Inversion parameters, diagnostics and global characteristics of the field models.

	Norm1	Norm 2	Norm 3	Norm 4
λ_s	8.0×10^2	8.0×10^2	4.0×10^2	8.0×10^6
rms misfit (nT)	26.11	26.09	26.5	26.39
Trace of R-Matrix	65	70	36	57
rms field intensity (nT)	331.19	332.75	327.05	335.24
g_1^0 (nT)	-217.5	-218.8	-213.8	-221.5
g_2^0/g_1^0	0.29	0.29	0.31	0.28
dipole tilt angle ($^\circ$)	0.6	0.4	0.7	0.8

215 4 Results

216 In this section, we present models of Mercury’s time-averaged magnetic field as they
 217 are based on MESSENGER measurements covering the period 2011-2015. We discuss
 218 to what extent our results are conclusive and estimate their robustness. The models pro-
 219 vide reasonably good fits to the data.

220 4.1 Resolution analysis and spectral content

221 For each of the four resulting models we computed the resolution matrix \mathbf{R} , and
 222 charted their diagonal elements, where labels of the models refer to the norm used to con-
 223 strain the solution, e.g. Norm 1 \rightarrow Model 1. These plots (resolution curves) are shown
 224 in Figure 1.

225 The resolution curves of all models generally agree for the first four spherical har-
 226 monic degrees. Most notable are the high resolution of sectorial Gauss coefficients, i.e.
 227 g_m^m, h_m^m , of at least the first five spherical harmonic degrees. Resolution curves of mod-
 228 els 1, 2 and 4 show this particular pattern also for higher spherical harmonic degrees,
 229 which may indicate a higher ability of these norms to capture small-scale magnetic field
 230 signatures. The higher resolution of the sectorial terms can be explained by MESSEN-
 231 GER’s flight path along latitude. We find that Model 3 resolves magnetic field structures
 232 only until spherical harmonic degree 4. The other models show resolution up to spher-

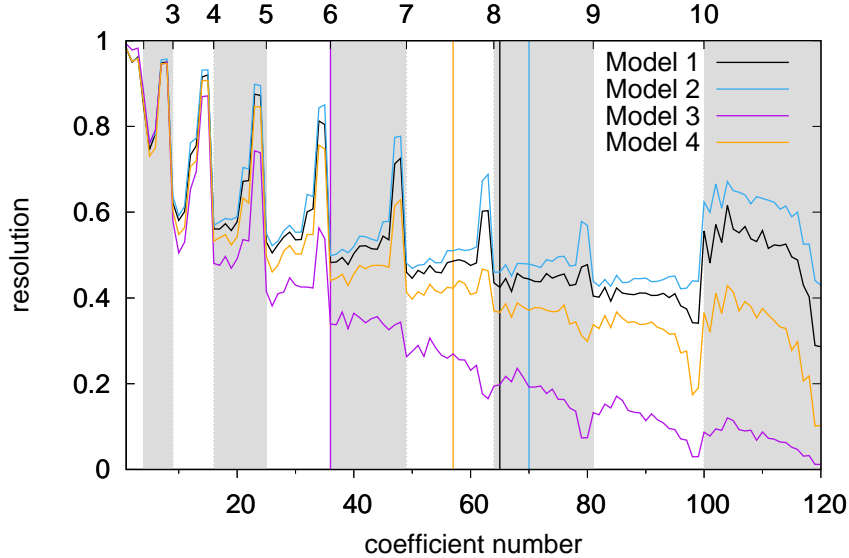


Figure 1. Diagonal elements of the resolution matrix of the preferred models for different priors vs. coefficient number (see also degree at the top axis). Gray shaded areas indicate even spherical harmonic degrees. The colored vertical lines represent the degree of freedom of the respective model.

233 ical harmonic degrees 6 (Model 4) and 7 (Models 1 and 2). For degrees 8 and 9 none of
 234 the models show resolution larger than 0.5. Below this level the model is dominated by
 235 the prior. At degree 10, i.e. coefficient numbers between 100 and 120, Models 1, 2 and
 236 4 show enhanced resolution, where they may become sensitive to spectral leakage, sig-
 237 nals of other sources and possible data errors. We assume the high resolution at these
 238 small scales to be an artifact and possibly caused by the orbital geometry of MESSENGER.
 239 Holme and Bloxham (1996) discussed a similar effect observed in the Voyager II
 240 data at Neptune, which was likely caused by the spacecraft trajectory. The truncation
 241 of the spherical harmonic expansion leads also to an aliasing of the higher degree field
 242 ($l > l_{\text{int}}$) into coefficients of the truncated spherical harmonic expansion (spectral leak-
 243 age). This effect is significantly reduced in Model 4, and therefore, we favor Model 4 as
 244 an optimal representation of Mercury’s core field up to spherical harmonic degree $l <$
 245 9.

246 Maps derived from truncated models ($l < 9$) of the radial magnetic field at the
 247 core surface are shown in Figure 2. As expected field structures in the northern hemi-
 248 sphere show more details than in the southern hemisphere, because of the data distri-

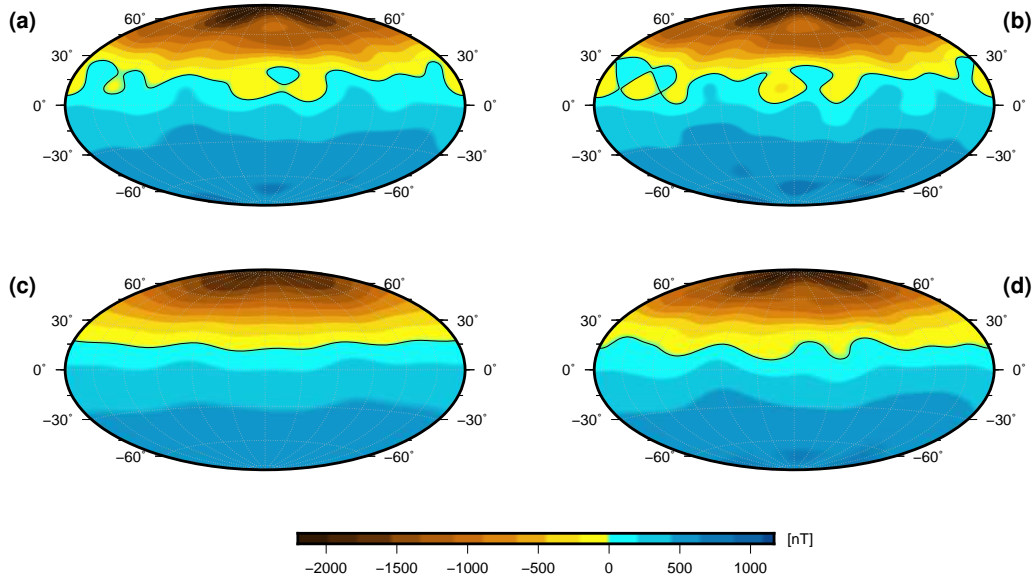


Figure 2. Radial component of the magnetic field at Mercury’s core surface of the selected model solutions: (a) Model 1, (b) Model 2, (c) Model 3 and (d) Model 4.

249 bution. Generally, the field is dominated by the axial dipole, but the magnetic equator
 250 is significantly shifted towards the North pole in agreement with previous studies (An-
 251 derson et al., 2011, 2012; Thébault et al., 2018). The different models show differing spa-
 252 tial complexities, in particular of the magnetic equator. The map derived with Norm 3
 253 shows the most axisymmetric field morphology, whereas models derived with Norms 1
 254 and 2 show more longitude-dependent structures including even some reversed flux patches.
 255 Overall, all models tend to agree in their large-scale structure (Table 1) and differ in their
 256 quantification of small scale features.

257 All models (1 - 4) show axial quadrupole-dipole ratios of 0.28-0.31 (Table 1) which
 258 are significantly smaller than those obtained by dipole offset models (Anderson et al.,
 259 2012; Johnson et al., 2012) but are in agreement with a model constructed using spher-
 260 ical caps (Thébault et al., 2018). We note that we could force the models to have a larger
 261 quadrupole-dipole ratio close to $g_2^0/g_1^0 = 0.4$; however, this leads to 10 - 20% larger rms
 262 misfits, which we consider to be significant and eventually deleterious for a large quadrupole-
 263 dipole ratio.

264 Maps in Figure 2 have also structures where no data are available, i.e. in the south-
 265 ern hemisphere. The magnetic field morphology in this hemisphere is mostly determined

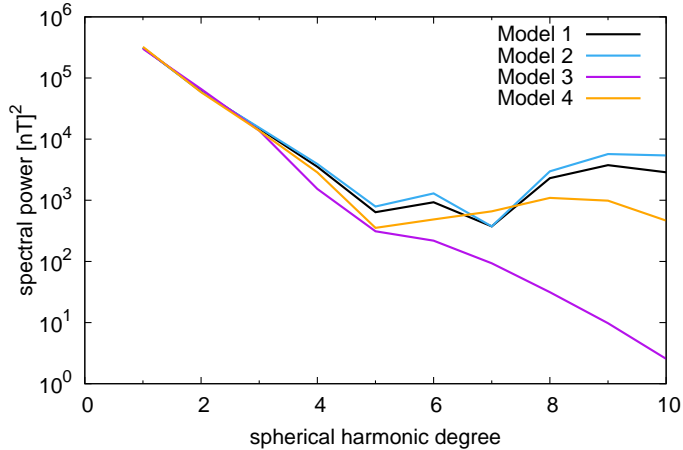


Figure 3. Power spectra of the four magnetic field models.

266 by the global characteristic of the spherical harmonic analysis and the prior used in the
 267 inversion. We, therefore do not attempt to interpret magnetic field features in the south-
 268 ern hemisphere.

269 Power spectra (Lowes, 1966; Mauersberger, 1956) of the models at the core sur-
 270 face are shown in Figure 3. The spectra mostly match for spherical harmonic degrees
 271 1 to 3. We find three different types of spectral slopes for spherical harmonic degrees $l >$
 272 5: decreasing, increasing and flat. The spectral power of Model 3 drops linearly, whereas
 273 Models 1 and 2 show powers that increase by one order of magnitude. Model 4 shows
 274 a flatter spectrum. This may lead to similar conclusions as taken from the resolution anal-
 275 ysis, where for Models 1, 2 and 4 spherical harmonic degrees above $l > 8$ may be in-
 276 fluenced by spectral leakage of magnetic small-scale sources close to the surface of Mer-
 277 cury.

278 The discussion of the spatial characteristic of Mercury’s steady magnetic field will
 279 therefore be based on Model 4 which is neither too damped (as Model 3) nor contam-
 280 inated by spectral leakage (as possibly Models 1 and 2).

281 4.2 Mercury’s time-averaged magnetic field

282 Maps in Figure 4 are derived from our preferred Model 4 until spherical harmonic
 283 degree 8. Figures 4a and b show the non-dipole field and the non-axisymmetric, i.e. non-
 284 zonal, field at Mercury’s core surface, respectively. The mapping of the non-dipole field

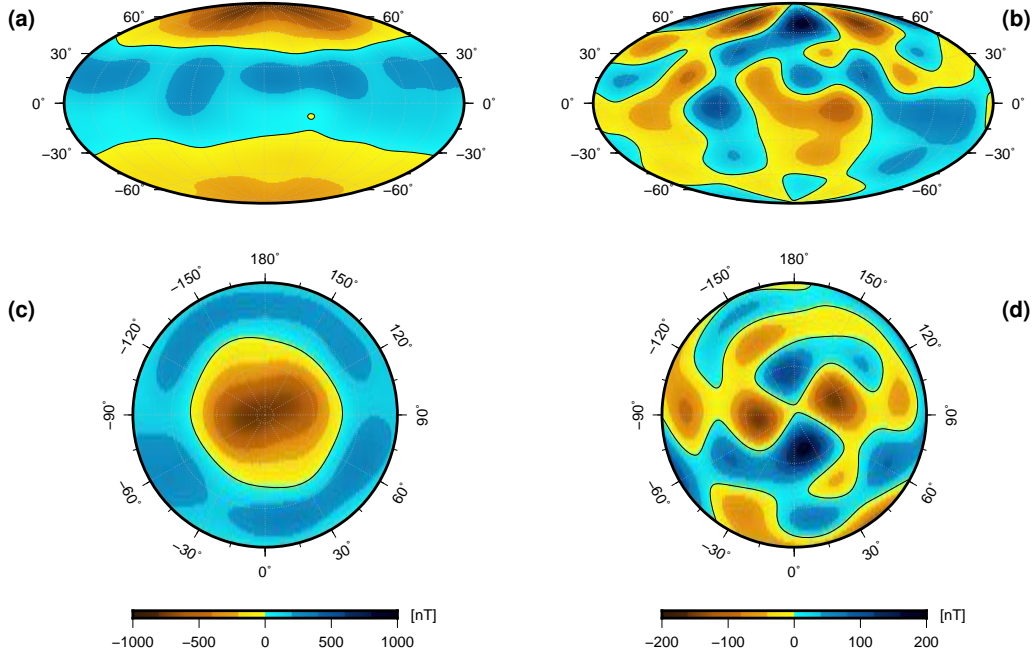


Figure 4. Radial component of: (a) the non-dipole and (b) the non-axisymmetric (non-zonal) magnetic field at Mercury’s core surface, respectively. (c) and (d) show north polar views of these magnetic field parts. Maps are derived using Model 4 up to spherical harmonic degree $l = 8$. The black lines mark the zero contour. Note different scales for maps (a), (c) and (b), (d).

285 excludes the dipole coefficients g_1^0, g_1^1 and h_1^1 , whereas the non-axisymmetric field excludes
 286 all zonal terms, i.e. g_l^0 . The non-dipole field (Figure 4a) is dominated by the equatorial-
 287 symmetric g_2^0 term. Though the estimate of g_2^0 is strongly influenced by the uneven dis-
 288 tribution of MESSENGER data, it is the second strongest coefficient of the field. In ad-
 289 dition, the field features at the northern hemisphere are stronger due to significant equatorial-
 290 antisymmetric terms, i.e. g_3^0 . Finally, the signature of two flux patches at northern high
 291 latitudes is evident in Figure 4b.

292 The polar view map of the non-dipole radial field at the surface of Mercury’s core
 293 (Figure 4c) shows an elongated patch of intense magnetic flux over the North pole. This
 294 pattern is surrounded by a region of positive (i.e. opposite polarity) magnetic flux with
 295 some intensified patterns, where the boundary between these regions of opposite polar-
 296 ity, i.e. the magnetic equator (black line) shows considerable undulations. These undu-
 297 lations further indicate non-axisymmetric field contributions.

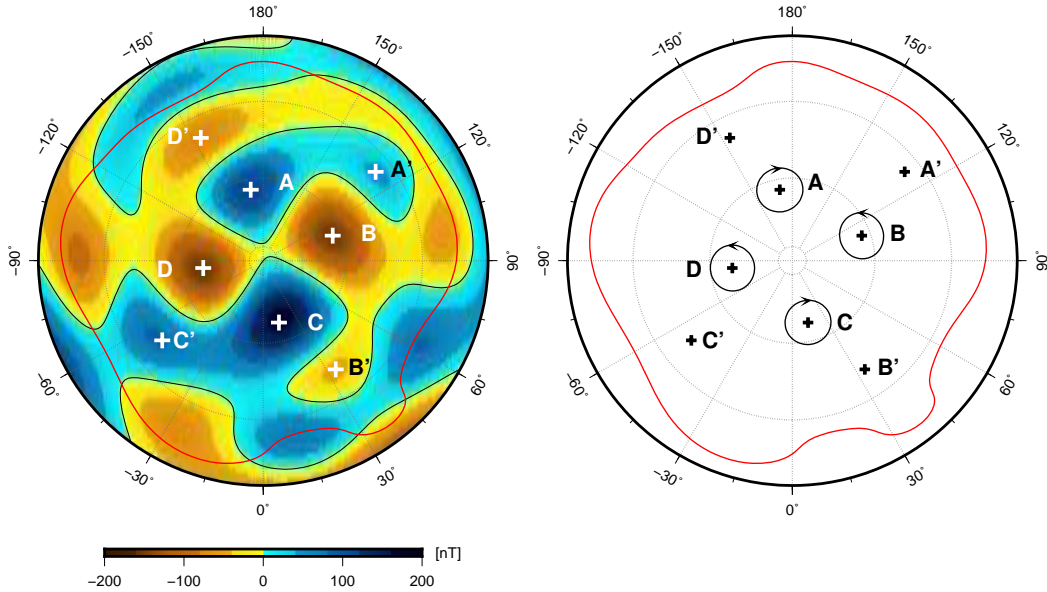


Figure 5. Polar view of the non-axisymmetric radial magnetic field at Mercury's core surface. The red line shows the position of the magnetic equator, capital letters mark apparent non-zonal field features and pluses their centers. Right: a schematic illustration of the individual convective rolls associated with the high-latitude non-zonal field features (clockwise A, C; counterclockwise B, D).

298 The non-zonal field, shown in Figures 4b and d, is fainter. Its amplitude ranges be-
 299 tween ± 200 nT, corresponding to $\sim 10\%$ of the total field. This part of the field allows
 300 unraveling longitude-dependent structures that are otherwise masked by the strong ax-
 301 isymmetric field. Particularly, the non-zonal field shows four features with alternating
 302 signs at high latitudes (A, B, C & D in Figure 5), indicative of two intense normal flux
 303 patches. The centers of these flux patches appear approximately at 65° northern lati-
 304 tude.

305 Finally, Mercury's core field also shows non-zonal structures at lower latitudes. These
 306 primed features (A', B', C' & D' in Figure 5) are weaker than their higher latitude coun-
 307 terparts. Moreover, the primed features do not correspond to any radial field structure
 308 of a certain polarity. The primed features seem to be shifted relatively to the higher lat-
 309 itude structures by a longitudinal angle of 30° to 60° to the west.

4.3 Inferring Mercury’s internal structure

The concentric arrangement of non-zonal features (A, B, C & D) in the northern hemisphere as seen in Figure 5 could be indicative of processes that are involved in the magnetic field generation. We assume that the nature of these features are linked to columnar rolls tangent to the inner core and parallel to the planet’s spin axis. Busse (1975) showed that such columnar flow exists when the Coriolis force dominates viscous and Lorentz forces in the convective region. Oppositely rotating convective rolls (clockwise and anticlockwise, see Figure 1 of Busse, 1975) may explain the different signs of the non-zonal magnetic field structures. Cyclones/anti-cyclones in the northern hemisphere correlate with convergence/divergence and concentrated/dispersed field, respectively (e.g. Olson et al., 1999). Accordingly, in Figure 5 the flux patches B & D may be concentrated by fluid downwellings associated with cyclones, while the positive non-zonal field (i.e. relatively weak field) in A & C may be dispersed by fluid upwellings associated with anti-cyclones.

We interpret the latitude of these flux patches by comparing to Earth’s magnetic core field. Amit et al. (2011) quantitatively identified centers of geomagnetic intense flux patches. Their Figure 9 and our Figure A.1 suggest that patch centers appear persistently at latitudes somewhat lower than that of the tangent cylinder. Analysis of the *gufm1* historical geomagnetic field model (Jackson et al., 2000) reveals that patch latitudes are time-dependent, appearing from about 30° latitude lower than the tangent cylinder until very close to it. However, in recent epochs when the field models are more reliable the patches reside less than ~10° lower than the tangent cylinder (Amit et al., 2011). This agrees with our analysis of a recent IGRF model (Thébault et al., 2015). The latitude of the geomagnetic flux patches based on Figure A.1 is approximately 8° lower than that of the tangent cylinder. We conclude that based on the behavior of the geomagnetic field the offset between the patches and the actual latitude where the tangent cylinder intersects the CMB is roughly $\delta\theta \sim 10^\circ \pm 10^\circ$.

Figure 6 (top) illustrates the classical tangent cylinder geometry with the addition of the effect of $\delta\theta$. This geometry is written as

$$\sin(\theta_{cmb} - \delta\theta) = \frac{r_i}{r_o}, \quad (6)$$

where r_i and r_o are the radii of the inner core and the CMB respectively. We assume that θ_{cmb} can be obtained from Mercury’s non-zonal field and that $\delta\theta$ is similar to Earth’s

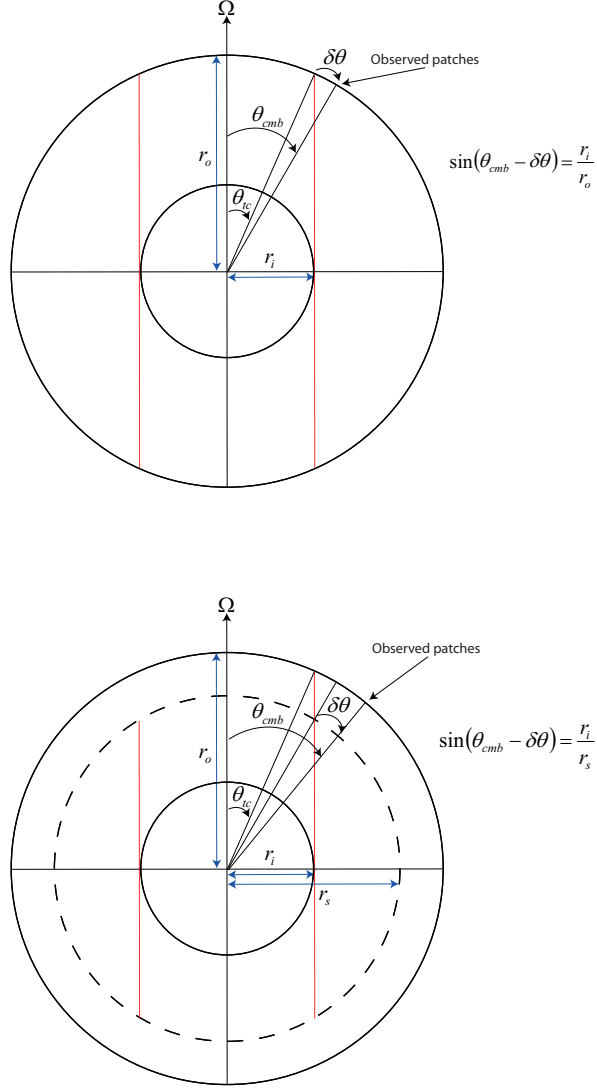


Figure 6. Schematic illustrations of the geometry of the tangent cylinder effect without (top) and with (bottom) a stably stratified layer. See text for the definitions of different angles.

341 value. This allows to derive r_i , Mercury’s inner core size. However, the presence of a strat-
 342 ified layer at the top of the core complicates this inference. When such a layer exists, the
 343 convective rolls concentrate flux at the base of the stratified layer, from which the skin
 344 effect carries the signal to the CMB by diffusion. Assuming that the signal propagation
 345 across the stratified layer is roughly radial, then Figure 6 (bottom) illustrates the rela-
 346 tion between the co-latitude of the patches θ_{cmb} , the radius of the inner core r_i and the
 347 radius of the base of the stratified layer r_s . Mathematically this relation is

$$\sin(\theta_{cmb} - \delta\theta) = \frac{r_i}{r_s}, \quad (7)$$

348 which contains two unknowns, r_i and r_s , and therefore cannot be uniquely determined.
 349 However, it provides a useful constraint and may be used to highlight various plausible
 350 scenarios for Mercury’s internal structure.

351 To estimate Mercury’s inner core size, we first estimate θ_{cmb} from Mercury’s mag-
 352 netic field model. The centers of intense flux patches B & D (Figure 5) reside at about
 353 latitude $\sim 65^\circ$ North, or co-latitude $\theta_{cmb} = 25^\circ$. From the analysis of the geomagnetic
 354 field we further assume $\delta\theta = 10^\circ \pm 10^\circ$. Substituting these values into (7) gives sce-
 355 narios for Mercury’s internal structure. Figure 7a presents the results for Mercury’s in-
 356 ner core size r_i and the thickness of the convective region is given in Figure 7b. Both are
 357 functions of the radius of the base of the stratified layer r_s , for three values of $\delta\theta$ which
 358 cover the considered range. Small values of r_s , which correspond to a very deep base of
 359 the layer (thick layer), give a very small inner core which would render the identifica-
 360 tion of a tangent cylinder effect to be impossible. Moreover, if most of the core is strat-
 361 ified, a dynamo action is unlikely. Larger values of r_s , which correspond to a thinner strat-
 362 ified layer, give a thicker inner core with stronger dependence on $\delta\theta$. For a thin strat-
 363 ified layer of ~ 50 km, with $\delta\theta = 0^\circ$ we find an upper bound $r_i \sim 850$ km and a con-
 364 vective region of 1160 km, with $\delta\theta = 10^\circ$ we find $r_i \sim 500$ km and a convective region
 365 of 1490 km, whereas with $\delta\theta = 20^\circ$ r_i is ~ 180 km (unlikely to be magnetically detectable)
 366 and a convective region of ~ 1830 km. On the other hand, with a thick stratified layer
 367 of ~ 1600 km for all $\delta\theta$ the inner core size is smaller than 200 km and the respective sizes
 368 of the active dynamo region are less than 400 km.

369 In the discussion section we elaborate on the consequences of the latitude of the
 370 magnetic flux patches on inferring the internal structure of Mercury.

371 5 Discussion

372 Figure 1 can directly be compared to results of a resolution analysis by Uno et al.
 373 (2009). The resolution of our preferred model is certainly higher than the resolution of
 374 their inversion results. This is mainly because of the wider spatial coverage during the
 375 MESSENGER main mission (2011 - 2015) than during the three flybys of Mariner-10
 376 and the one MESSENGER flyby in 2008. However, Uno et al. (2009) concluded that a
 377 realistic resolution up to spherical harmonic degree 10 can be obtained from the flyby
 378 data. We consider this as an optimistic view, as it (implicitly) assumes that model pa-

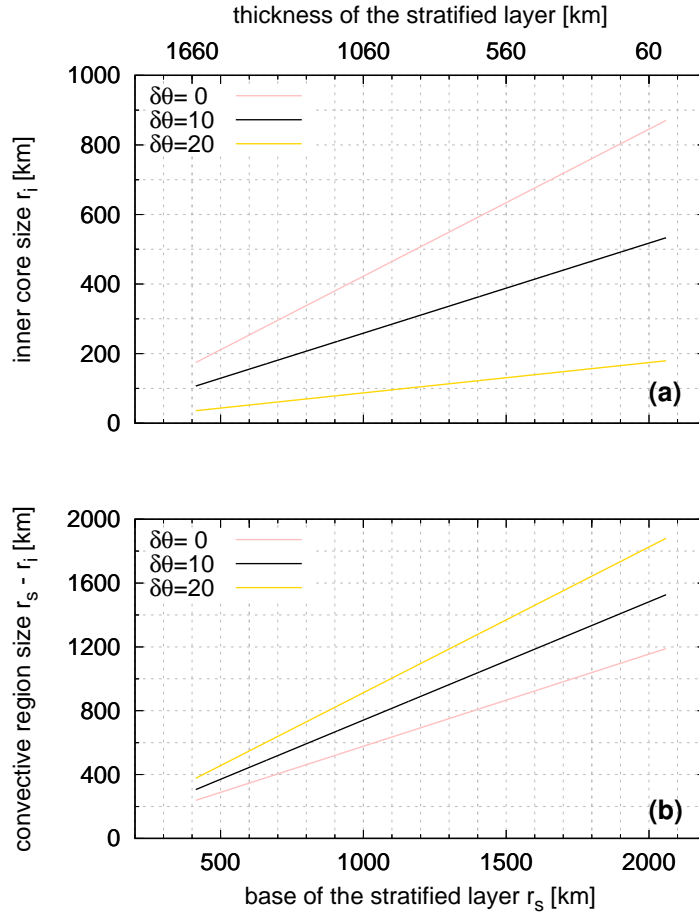


Figure 7. Mercury's inner core size r_i (a) and the thickness of the convective region (b) vs. the radius of the base of the stratified layer r_s (or the layer thickness, see top horizontal scale), for three values of $\delta\theta$ (see legend).

rameters with a small but non-zero resolution can be resolved by the inversion. In this respect, we are cautious in choosing a minimum resolution R_{\min} which would be relevant for robust results. We find that a value of $R_{\min} \geq 0.4$ is a diligent choice for a required minimum resolution. The model solutions 1, 2 and 4 largely meet this criterion, and maps of these models are in good agreement when truncated to spherical harmonic degree $l < 9$. However, we focus on magnetic field Model 4 in the following, because Models 1 and 2 tend to show small-scale structures along the magnetic equator that arise from spherical harmonic degrees $l > 8$ which we consider uncertain.

Our analysis reveals features of Mercury’s magnetic core field that could provide insights to characterize the planet’s internal structure and the dynamo action in its core. The morphology of Mercury’s non-axisymmetric magnetic field that is shown in Figures 4b and d resembles (perhaps incidentally) the geomagnetic field in the form of two high-latitude normal flux patches (e.g. Gubbins, 2003; Jackson et al., 2000). The axisymmetric and non-axisymmetric parts of Mercury’s magnetic field may be due to different processes. In this context it has been proposed that a stratified layer outside the dynamo region of Saturn leads to the axisymmetrization of its magnetic field (Stevenson, 1982; Stanley, 2010). Similar mechanisms are likely to be at work inside Mercury (Christensen, 2006; Christensen & Wicht, 2008).

Mercury’s internal structure is still unresolved by geodetic analyses and there is a debate concerning the existence and possible size of a solid inner core. If a solid inner core exists, it was argued that its radius is likely to be smaller than ~ 1000 km (Van Hoolst et al., 2012; Cao et al., 2014; Dumberry & Rivoldini, 2015; Peale et al., 2016). Based on estimates of Mercury’s gravity field, tidal Love number and pole coordinates, Mercury’s inner core radius is in the range 883 to 1026 km (Genova et al., 2019). However, reported values of Mercury’s inner core size are still under debate and estimates derived from a geodetic analysis of Mercury’s orbital motion give a larger range of 370-1200 km (from combining the first and third quartiles of Margot et al., 2018).

Based on the above estimates from geodetic analyses we consider Mercury’s inner core size to be $r_i = 500$ -1000 km. For $r_i = 500$ km and $\delta\theta = 0^\circ$ Figure 7(a) gives a stratified layer thickness of ~ 880 km which leaves ~ 680 km for the convective region to maintain a dynamo. For $r_i = 500$ km and $\delta\theta = 10^\circ$ the stratified layer thickness is ~ 130 km and the convective region is ~ 1430 km, while for $r_i = 500$ km and $\delta\theta = 20^\circ$ a so-

411 lution does not exist. Furthermore, an inner core size of $r_i = 1000$ km is out of range
 412 for the considered $\delta\theta$ values (Figure 7(a)). Because the large scale field of Mercury fa-
 413vors a substantial stratified layer, and because large r_i constrains $\delta\theta$ to small admissi-
 414ble values, we conclude that the inner core size tends towards the small end of the con-
 415sidered r_i range.

416 The thickness of the stratified layer at the top of Mercury’s core is also unknown.
 417 Smith et al. (2012) suggested that a 200 km thick and solid FeS-layer at the interface
 418 of a silicate mantle and the metallic core may explain the planet’s moment of inertia.
 419 However, this setup was questioned by Hauck et al. (2013) who derived models without
 420 an FeS-layer to reproduce the gravity field observations and libration data. The thick-
 421ness of such a layer depends on the available Sulfur and its solubility in the metallic core
 422determined by the widely unknown core temperature and reduction conditions (Hauck
 423et al., 2013). In most numerical dynamo simulations that attempt to explain observa-
 424tions of Mercury’s magnetic field a thick layer is assumed, from several hundred km (e.g.
 425600 km in Christensen, 2006; Christensen & Wicht, 2008) up to half the core radius (Taka-
 426hashi et al., 2019). The stratified layer weakens and diffuses the non-axisymmetric field
 427via a skin effect, which could explain its low intensity and dominant axisymmetry.

428 Considering a stratified layer thickness of 500-1000 km (or $r_s = 1560-1060$ km), we
 429 obtain $r_i \sim 660-90$ km and a dynamo region of $\sim 1420-610$ km, respectively with ranges
 430 corresponding to the different $\delta\theta$ values (Figure 7). The small inner core scenario (with
 431 $\delta\theta = 20^\circ$) seems unlikely to produce a detectable tangent cylinder effect. We therefore
 432 favor again the solutions for low $\delta\theta$ which correspond here to inner core sizes of $\sim 660-$
 433450 km and convective region sizes of approximately 900-610 km.

434 6 Conclusion

435 In this study, we investigate the morphology of Mercury’s magnetic core field and
 436 the smallest possible spatial scales that can be resolved from the MESSENGER mea-
 437surements. Our spherical harmonic analysis demonstrates that features of the time-averaged
 438magnetic core field of spherical harmonic degree $l = 8$ can be robustly resolved, inde-
 439pendent of the model prior. Higher spherical harmonic degrees are likely aliased by un-
 440determined magnetic signatures. Moreover, we detect non-axisymmetric features of the

441 core magnetic field that are absent in the dipole offset model (Anderson et al., 2012; John-
 442 son et al., 2012).

443 For the first time, Mercury’s non-axisymmetric core field is identified and studied
 444 to infer the internal structure of its core. We find non-axisymmetric flux patches at high
 445 northern latitudes. We interpret these features as the signature of convective columns
 446 adjacent to the inner core tangent cylinder. The deviation from axisymmetry introduced
 447 by these patches is far less pronounced than at Earth’s geomagnetic field due to the mask-
 448 ing by Mercury’s dominant axisymmetric field.

449 We take advantage of the mean latitude of these two patches to constrain Mercury’s
 450 internal structure. We establish a relation between the inner core size and the thickness
 451 of the stratified layer below the CMB as a function of the latitude of the magnetic flux
 452 patches. While various combinations of these two quantities are possible, a combined in-
 453 terpretation of our results and those from geodetic analyses limits the range of the in-
 454 ner core radius to $\sim 500\text{-}660$ km. Accordingly the stratified layer thickness is $\sim 880\text{-}500$
 455 km, leaving $\sim 900\text{-}610$ km for the convective dynamo region, respectively. Furthermore,
 456 our results favor little (if any) shift between the locations of magnetic flux patches and
 457 the tangent cylinder at the top of the dynamo region, in apparent contrast to the off-
 458 set observed at Earth’s core.

459 Finally we emphasize that our analysis is based on a data set of the MESSENGER
 460 mission over the northern hemisphere only. This puts limits on the magnetic field mod-
 461 els and the inferences concerning Mercury’s internal structure. The future Bepi-Colombo
 462 mission will unravel these details of Mercury’s magnetic core field.

463 **Acknowledgments**

464 The MESSENGER mission was supported by the NASA Discovery Program under con-
 465 tracts NAS5-97271 to The Johns Hopkins University Applied Physics Laboratory and
 466 NASW-00002 to the Carnegie Institution of Washington. All MESSENGER data used
 467 here are publicly available on NASA’s Planetary Data System (PDS) at [http://ppi.pds](http://ppi.pds.nasa.gov)
 468 [.nasa.gov](http://ppi.pds.nasa.gov). This research was supported by the French Agence Nationale de la Recherche,
 469 project MARMITE, contract 654 ANR-13-BS05-0012, as well as by Centre National des
 470 Etudes Spatiales in the context of the BepiColombo MAG experiment. We would like

471 to thank J. Wicht for suggesting to test for models with larger quadrupole-dipole ratio.
 472 All graphics were produced using opensource software, GMT and gnuplot.

473 The authors declare that they have no competing interests.

474 References

- 475 Amit, H., Aubert, J., & Hulot, G. (2010, Jul). Stationary, oscillating or drifting
 476 mantle-driven geomagnetic flux patches? *Journal of Geophysical Research*
 477 (*Solid Earth*), *115*(B7), B07108. doi: 10.1029/2009JB006542
- 478 Amit, H., Korte, M., Aubert, J., Constable, C., & Hulot, G. (2011, December). The
 479 time-dependence of intense archeomagnetic flux patches. *Journal of Geophysi-*
 480 *cal Research (Solid Earth)*, *116*(B12), B12106. doi: 10.1029/2011JB008538
- 481 Anderson, B. J., Acuña, M. H., Lohr, D. A., Scheifele, J., Raval, A., Korth, H., &
 482 Slavin, J. A. (2007). The Magnetometer Instrument on MESSENGER. *Space*
 483 *Science Reviews*, *131*(1), 417–450. doi: 10.1007/s11214-007-9246-7
- 484 Anderson, B. J., Johnson, C. L., Korth, H., Purucker, M. E., Winslow, R. M.,
 485 Slavin, J. A., ... Zurbuchen, T. H. (2011, Sep). The Global Magnetic Field of
 486 Mercury from MESSENGER Orbital Observations. *Science*, *333*(6051), 1859.
 487 doi: 10.1126/science.1211001
- 488 Anderson, B. J., Johnson, C. L., Korth, H., Winslow, R. M., Borovsky, J. E., Pu-
 489 rucker, M. E., ... McNutt, R. L., Jr. (2012, December). Low-degree structure
 490 in Mercury’s planetary magnetic field. *Journal of Geophysical Research (Plan-*
 491 *ets)*, *117*, E00L12. doi: 10.1029/2012JE004159
- 492 Bloxham, J., & Gubbins, D. (1987). Thermal core-mantle interactions. *Nature*, *325*,
 493 511-513.
- 494 Bloxham, J., Gubbins, D., & Jackson, A. (1989). Geomagnetic secular variation.
 495 *Philos. Trans. R. Soc. London A*, *329*, 415-502.
- 496 Busse, F. H. (1975, January). A model of the geodynamo. *Geophys. J. Int.*, *42*, 437-
 497 459. doi: 10.1111/j.1365-246X.1975.tb05871.x
- 498 Cao, H., Aurnou, J. M., Wicht, J., Dietrich, W., Soderlund, K. M., & Russell, C. T.
 499 (2014, June). A dynamo explanation for Mercury’s anomalous magnetic field.
 500 *Geophys. Res. Lett.*, *41*(12), 4127-4134. doi: 10.1002/2014GL060196
- 501 Christensen, U. (2006, December). A deep dynamo generating Mercury’s magnetic
 502 field. *Nature*, *444*, 1056-1058. doi: 10.1038/nature05342

- 503 Christensen, U., Olson, P., & Glatzmaier, G. A. (1998, January). A dynamo model
504 interpretation of geomagnetic field structures. *Geophys. Res. Lett.*, *25*(10),
505 1565-1568. doi: 10.1029/98GL00911
- 506 Christensen, U., & Wicht, J. (2008, July). Models of magnetic field generation
507 in partly stable planetary cores: Applications to Mercury and Saturn. *Icarus*,
508 *196*, 16-34. doi: 10.1016/j.icarus.2008.02.013
- 509 Connerney, J. E. P., & Ness, N. F. (1988). Mercury's magnetic field and interior.
510 In F. Vilas, C. R. Chapman, & M. S. Matthews (Eds.), *Mercury, university of*
511 *arizona press* (p. 494-513).
- 512 Dumberry, M., & Rivoldini, A. (2015, Mar). Mercury's inner core size and core-
513 crystallization regime. *Icarus*, *248*, 254-268. doi: 10.1016/j.icarus.2014.10.038
- 514 Genova, A., Goossens, S., Mazarico, E., Lemoine, F. G., Neumann, G. A., Kuang,
515 W., ... Zuber, M. T. (2019, Apr). Geodetic Evidence That Mercury
516 Has A Solid Inner Core. *Geophys. Res. Lett.*, *46*(7), 3625-3633. doi:
517 10.1029/2018GL081135
- 518 Gubbins, D. (1975). Can the Earth's magnetic field be sustained by core oscilla-
519 tions? *Geophys. Res. Lett.*, *2*, 409-412.
- 520 Gubbins, D. (1983). Geomagnetic field analysis – I. Stochastic inversion. *Geophys. J.*
521 *R. astr. Soc.*, *73*, 641-652.
- 522 Gubbins, D. (2003). Thermal core-mantle interactions: Theory and observations. In
523 V. Dehant, K. Creager, S. Karato, & S. Zatman (Eds.), *Earths Core: Dynam-*
524 *ics, Structure and Rotation*. American Geophysical Union.
- 525 Gubbins, D., & Bloxham, J. (1987). Morphology of the geomagnetic field and impli-
526 cations for the geodynamo. *Nature*, *325*, 509-511.
- 527 Hauck, S. A., Margot, J.-L., Solomon, S. C., Phillips, R. J., Johnson, C. L.,
528 Lemoine, F. G., ... Zuber, M. T. (2013, Jun). The curious case of Mer-
529 cury's internal structure. *Journal of Geophysical Research (Planets)*, *118*(6),
530 1204-1220. doi: 10.1002/jgre.20091
- 531 Holme, R., & Bloxham, J. (1996). The magnetic fields of Uranus and Neptune:
532 Methods and models. *J. geophys. Res.*, *101*, 2177-2200.
- 533 Jackson, A., Jonkers, A. R. T., & Walker, M. R. (2000). Four centuries of geomag-
534 netic secular variation from historical records. *Phil. Trans. R. Soc. Lond. A*,
535 *358*, 957-990.

- 536 Jackson, D. D. (1979). The use of a priori data to resolve nonuniqueness in linear in-
537 version. *Geophys. J. R. astr. Soc.*, *57*, 137-157.
- 538 Johnson, C. L., Purucker, M. E., Korth, H., Anderson, B. J., Winslow, R. M., Al
539 Asad, M. M. H., . . . Solomon, S. C. (2012, December). MESSENGER obser-
540 vations of Mercury's magnetic field structure. *Journal of Geophysical Research*
541 (*Planets*), *117*, E00L14. doi: 10.1029/2012JE004217
- 542 Lowes, F. J. (1966). Mean-square values on sphere of spherical harmonic vector
543 fields. *J. geophys. Res.*, *71*, 2179.
- 544 Manglik, A., Wicht, J., & Christensen, U. R. (2010, January). A dynamo model
545 with double diffusive convection for Mercury's core. *Earth and Planetary Sci-*
546 *ence Letters*, *289*(3-4), 619-628. doi: 10.1016/j.epsl.2009.12.007
- 547 Margot, J.-L., Hauck, I., Steven A., Mazarico, E., Padovan, S., & Peale, S. J. (2018,
548 June). Mercury's Internal Structure. *arXiv e-prints*, arXiv:1806.02024.
- 549 Mauersberger, P. (1956). Das Mittel der Energiedichte des geomagnetischen Haupt-
550 feldes an der Erdoberfläche und seine säkulare Änderung. *Gerlands Beiträge*
551 *zur Geophysik*, *65*, 207-215.
- 552 Ness, N. F. (1979, November). The magnetic field of Mercury. *Phys. Earth Planet.*
553 *Inter.*, *20*, 209-217. doi: 10.1016/0031-9201(79)90044-X
- 554 Ness, N. F., Behannon, K. W., Lepping, R. P., Whang, Y. C., & Schatten, K. H.
555 (1974, July). Magnetic Field Observations near Mercury: Preliminary Results
556 from Mariner 10. *Science*, *185*, 151-160. doi: 10.1126/science.185.4146.151
- 557 Oliveira, J. S., Hood, L. L., & Langlais, B. (2019, Sep). Constraining the Early
558 History of Mercury and Its Core Dynamo by Studying the Crustal Magnetic
559 Field. *Journal of Geophysical Research (Planets)*, *124*(9), 2382-2396. doi:
560 10.1029/2019JE005938
- 561 Oliveira, J. S., Langlais, B., Pais, M. A., & Amit, H. (2015, June). A modified
562 Equivalent Source Dipole method to model partially distributed magnetic field
563 measurements, with application to Mercury. *Journal of Geophysical Research*
564 (*Planets*), *120*, 1075-1094. doi: 10.1002/2014JE004734
- 565 Olson, P., Christensen, U., & Glatzmaier, G. A. (1999). Numerical modeling of
566 the geodynamo: Mechanisms of field generation and equilibration. *J. geophys.*
567 *Res.*, *104*, 10383-10404. doi: 10.1029/1999JB900013
- 568 Olson, P., Landeau, M., & Reynolds, E. (2018, Oct). Outer core stratification

- 569 from the high latitude structure of the geomagnetic field. *Frontiers in Earth*
570 *Science*, 6, 140. doi: 10.3389/feart.2018.00140
- 571 Panovska, S., Korte, M., & Constable, C. G. (2019, Dec). One Hundred Thou-
572 sand Years of Geomagnetic Field Evolution. *Reviews of Geophysics*, 57(4),
573 1289-1337. doi: 10.1029/2019RG000656
- 574 Peña, D., Amit, H., & Pinheiro, K. J. (2016, May). Magnetic field stretching at the
575 top of the shell of numerical dynamos. *Earth, Planets, and Space*, 68(1), 78.
576 doi: 10.1186/s40623-016-0453-x
- 577 Peale, S. J., Margot, J.-L., Hauck, S. A., & Solomon, S. C. (2016, Jan). Conse-
578 quences of a solid inner core on Mercury's spin configuration. *Icarus*, 264, 443-
579 455. doi: 10.1016/j.icarus.2015.09.024
- 580 Shure, L., Parker, R. L., & Backus, G. E. (1982). Harmonic splines for geomagnetic
581 modelling. *Phys. Earth Planet. Inter.*, 28, 215-229.
- 582 Smith, D. E., Zuber, M. T., Phillips, R. J., Solomon, S. C., Hauck, S. A., Lemoine,
583 F. G., ... Taylor, A. H. (2012, Apr). Gravity Field and Internal Struc-
584 ture of Mercury from MESSENGER. *Science*, 336(6078), 214. doi:
585 10.1126/science.1218809
- 586 Stanley, S. (2010, March). A dynamo model for axisymmetrizing Saturn's magnetic
587 field. *Geophys. Res. Lett.*, 37(5), L05201. doi: 10.1029/2009GL041752
- 588 Stanley, S., Bloxham, J., Hutchison, W. E., & Zuber, M. T. (2005, May). Thin shell
589 dynamo models consistent with Mercury's weak observed magnetic field. *Earth*
590 *and Planetary Science Letters*, 234, 27-38. doi: 10.1016/j.epsl.2005.02.040
- 591 Stanley, S., & Mohammadi, A. (2008, Jul). Effects of an outer thin stably strati-
592 fied layer on planetary dynamos. *Phys. Earth Planet. Inter.*, 168(3-4), 179-190.
593 doi: 10.1016/j.pepi.2008.06.016
- 594 Stevenson, D. J. (1982, January). Reducing the non-axisymmetry of a planetary
595 dynamo and an application to saturn. *Geophys. Astrophys. Fluid Dyn.*, 21(1),
596 113-127. doi: 10.1080/03091928208209008
- 597 Takahashi, F., Shimizu, H., & Tsunakawa, H. (2019, January). Mercury's anomalous
598 magnetic field caused by a symmetry-breaking self-regulating dynamo. *Nature*
599 *Communications*, 10, 208. doi: 10.1038/s41467-018-08213-7
- 600 Tarantola, A. (1987). *Inverse problem theory. Methods for data fitting and model pa-*
601 *rameter estimation*. Amsterdam: Elsevier, 1987.

- 602 Thébault, E., Finlay, C. C., Beggan, C. D., Alken, P., Aubert, J., Barrois, O., ...
603 Zvereva, T. (2015). International Geomagnetic Reference Field: the 12th gen-
604 eration. *Earth, Planets, and Space*, *67*, 79. doi: 10.1186/s40623-015-0228-9
- 605 Thébault, E., Langlais, B., Oliveira, J. S., Amit, H., & Leclercq, L. (2018, March).
606 A time-averaged regional model of the Hermean magnetic field. *Phys. Earth*
607 *Planet. Inter.*, *276*, 93-105. doi: 10.1016/j.pepi.2017.07.001
- 608 Tian, Z., Zuber, M. T., & Stanley, S. (2015, November). Magnetic field modeling for
609 Mercury using dynamo models with a stable layer and laterally variable heat
610 flux. *Icarus*, *260*, 263-268. doi: 10.1016/j.icarus.2015.07.019
- 611 Uno, H., Johnson, C. L., Anderson, B. J., Korth, H., & Solomon, S. C. (2009,
612 August). Modeling Mercury's internal magnetic field with smooth inver-
613 sions. *Earth and Planetary Science Letters*, *285*, 328-339. doi: 10.1016/
614 j.epsl.2009.02.032
- 615 Van Hoolst, T., Rivoldini, A., Baland, R.-M., & Yseboodt, M. (2012, Jun).
616 The effect of tides and an inner core on the forced longitudinal libra-
617 tion of Mercury. *Earth and Planetary Science Letters*, *333*, 83-90. doi:
618 10.1016/j.epsl.2012.04.014
- 619 Wardinski, I., Langlais, B., & Thbault, E. (2019). Correlated time-varying magnetic
620 fields and the core size of mercury. *Journal of Geophysical Research: Planets*,
621 *124*(8), 2178-2197. doi: 10.1029/2018JE005835
- 622 Winslow, R. M., Anderson, B. J., Johnson, C. L., Slavin, J. A., Korth, H., Purucker,
623 M. E., ... Solomon, S. C. (2013). Mercury's magnetopause and bow shock
624 from MESSENGER Magnetometer observations. *J. Geophys. Res.*, *118*. doi:
625 10.1002/jgra.50237

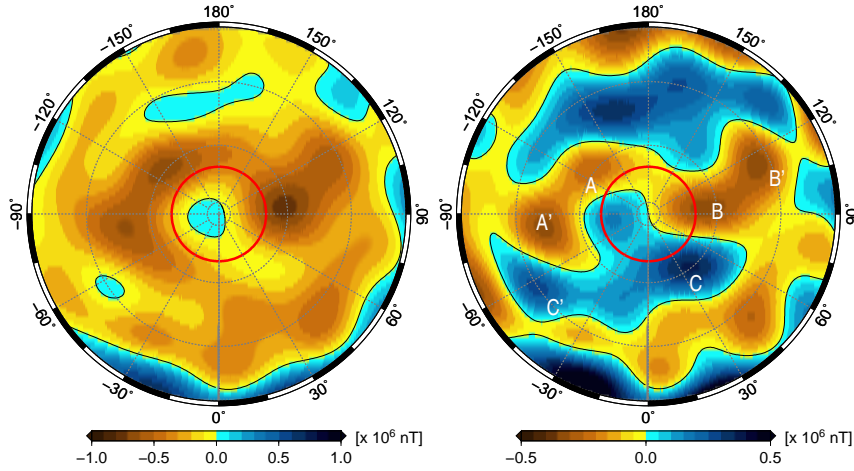


Figure A.1. North polar views of the radial magnetic field component (left) and its non-axisymmetric part (right) at Earth's core surface. The red circles represent the diameter of Earth's inner core.

A Earth's core field

Figure A.1 shows the radial geomagnetic field component and its non-axisymmetric part at Earth's core surface in the year 2015. The maps are based on the 12th International geomagnetic reference field (Thébault et al., 2015). The model was truncated at spherical harmonic degree $l = 10$. The maps show also the projection of the inner core tangent cylinder on the CMB.